

# Topological states and topological phase transition in $\text{Cu}_2\text{SnS}_3$ and $\text{Cu}_2\text{SnSe}_3$

Li Qin Zhou,<sup>1,2</sup> Yuting Qian,<sup>1,2</sup> Changming Yue,<sup>3</sup> Zhong Fang,<sup>1,2</sup> Wei Zhang,<sup>4,5,\*</sup> Chen Fang,<sup>1,2,†</sup> and Hongming Weng<sup>1,2,6,‡</sup>

<sup>1</sup>Beijing National Laboratory for Condensed Matter Physics and Institute of physics, Chinese academy of sciences, Beijing 100190, China

<sup>2</sup>University of Chinese academy of sciences, Beijing 100049, China

<sup>3</sup>Department of Physics, University of Fribourg, 1700 Fribourg, Switzerland

<sup>4</sup>Fujian Provincial Key Laboratory of Quantum Manipulation and New Energy Materials,  
College of Physics and Energy, Fujian Normal University, Fuzhou 350117, China

<sup>5</sup>Fujian Provincial Collaborative Innovation Center for Advanced High-Field  
Superconducting Materials and Engineering, Fuzhou 350117, China

<sup>6</sup>Songshan Lake Materials Laboratory, Dongguan, Guangdong 523808, China

Based on the first-principles calculations within local density approximation and model analysis, we propose that the iso-structural compounds  $\text{Cu}_2\text{SnS}_3$  and  $\text{Cu}_2\text{SnSe}_3$  are both the simplest nodal line semimetals with only one nodal line in their crystal momentum space when spin-orbit coupling (SOC) is ignored. The including of SOC drives  $\text{Cu}_2\text{SnS}_3$  into a Weyl semimetal (WSM) state with only two pairs of Weyl nodes, the minimum number required for WSM with time reversal symmetry. In contrast, SOC leads  $\text{Cu}_2\text{SnSe}_3$  to strong topological insulator (TI) state. This difference can be well understood as there is a topological phase transition (TPT). In it, the Weyl nodes are driven by tunable SOC and annihilate in a mirror plane, resulting in a TI. This TPT, together with the evolution of Weyl nodes, the changing of mirror Chern numbers of mirror plane and the  $Z_2$  indices protected by time-reversal symmetry has been demonstrated by the calculation of  $\text{Cu}_2\text{SnS}_{3-x}\text{Se}_x$  within virtual crystal approximation and an effective  $k \cdot p$  model analysis. Though our first-principles calculations have overestimated the topological states in both compounds, we believe that the theoretical demonstration of controlling TPT and evolution of Weyl nodes will stimulate further efforts in exploring them.

## I. INTRODUCTION

After nearly fifteen years development, the classification of topological electronic bands and their topological materials have been quite well developed.<sup>1-9</sup> The gapped states have been classified both with internal and spatial symmetries. The internal symmetries include time-reversal symmetry, chiral (sub-lattice) symmetry and particle-hole symmetry and the spatial symmetries include the crystalline symmetries in all four types of magnetic space groups. The Chern insulator, integer quantum anomalous Hall insulator, topological insulator (TI), topological crystalline insulator (TCI) as well as topological superconductor belong to these classifications. For the metals, the topological classification has been done mainly according to the nodal points close to Fermi energy. According to the degeneracy, topological charge and distribution of these nodes, there have been Weyl semimetal (WSM), Dirac semimetal (DSM), topological nodal-line semimetal (TNLS) and multiple-degeneracy nodal point semimetal.<sup>10-24</sup> Topological semimetal phases can be viewed as the intermediate states in the process of the topological phase transition (TPT) between different topological phases, such as the normal insulator (NI) to TI, which has been systematically studied by Murakami *et al.*<sup>25-31</sup> In inversion-symmetric systems, the conduction band and valence band gradually approach each other in the phase transition process, and the band gap closes at time-reversal invariant momenta (TRIM) only, where a four-fold degenerate Dirac nodes appeared. The intermediate state of the phase transition is a DSM phase, but as a critical point it is unstable and easy to be destroyed. On the other hand, for inversion-asymmetric systems, the band gap will close at certain  $k$ -point away from TRIM and at least two pairs of Weyl nodes with opposite chirality will emerge as constrained by time-reversal symmetry (TRS) and no-go theorem. This in-

intermediate state of the phase transition is a WSM phase. The Weyl nodes are separated in reciprocal space and they should appear and disappear in pair when tuning one or more parameters in the Hamiltonian properly. In this sense, the intermediate WSM phase can not be destroyed immediately and it is relatively robust against perturbation, facilitating the material realization.

In this work, we have theoretically investigated two iso-structural compounds  $\text{Cu}_2\text{SnS}_3$  and  $\text{Cu}_2\text{SnSe}_3$ . We find they are very suitable to study the TPT from a WSM to a TI. When spin-orbit coupling (SOC) is ignored, both of them are nodal line semimetal with only one nodal ring around the Fermi energy lying in one mirror plane. When SOC is considered,  $\text{Cu}_2\text{SnS}_3$  becomes a WSM with two pairs of Weyl nodes, while  $\text{Cu}_2\text{SnSe}_3$  is a strong TI. The evolution and annihilation of Weyl nodes in this iso-structural and iso-electronic family compounds can be demonstrated by systematically tuning the effective SOC. To do this, we employ the virtual crystal approximation (VCA) method to simulate the different Se doping concentration of  $\text{Cu}_2\text{SnS}_{3-x}\text{Se}_x$ . Since there are no topologically nontrivial symmetry-based indicators in their space group  $Imm2$  (No. 44) to directly judge their topological classification,<sup>2,32,33</sup> we characterize their topological states by calculating the mirror Chern number (MCN) for two mutually perpendicular mirror planes and  $Z_2$  indices according to the Wilson loop method.<sup>34,35</sup> To reveal the mechanism of TPT, an effective  $k \cdot p$  model has been constructed and analyzed according to the representations of the bands forming the nodal ring and Weyl nodes. In the following, we firstly introduce the calculation method, and then discuss the topological states of  $\text{Cu}_2\text{SnS}_3$  and  $\text{Cu}_2\text{SnSe}_3$  without and with SOC, respectively. Finally, the TPT from WSM in  $\text{Cu}_2\text{SnS}_3$  to TI of  $\text{Cu}_2\text{SnSe}_3$  has been investigated systematically.

## II. METHOD

The density functional theory (DFT) calculation of the electronic structures for  $\text{Cu}_2\text{SnS}_3$  and  $\text{Cu}_2\text{SnSe}_3$  are performed by using the Vienna *ab initio* simulation package (VASP)<sup>36</sup>. The generalized gradient approximation (GGA) with the Perdew-Burke-Ernzerhof (PBE) functional are selected to describe the exchange-correlation energy<sup>37,38</sup>. The cutoff energy for plane-wave basis is set to 520 eV and the reciprocal space is sampled by  $11 \times 11 \times 11$   $\Gamma$ -centered  $k$  mesh. To further calculate the topological properties of  $\text{Cu}_2\text{SnS}_3$  and  $\text{Cu}_2\text{SnSe}_3$  such as surface states and MCN, we have constructed the tight-binding model with the maximally-localized Wannier functions (MLWF)<sup>39</sup> generated for Cu 3d, Sn 5s+p and S (Se) 3p (4p) orbitals. The surface states and Fermi arcs are calculated by using the WannierTools package<sup>40</sup>, which based on the surface Green's function method. In order to study the TPT process between  $\text{Cu}_2\text{SnS}_3$  and  $\text{Cu}_2\text{SnSe}_3$ , we use the VCA method (suppose different proportions of S and Se atoms occupy simultaneously the same atomic sites) to calculate the band structures with different S:Se ratios. Similary, we mix linearly the above tight-binding Hamiltonian based on Wannier functions of the two parent compounds to obtain the Hamiltonian of the doped one, which is found to be efficient in further determining the phase transition critical point and the evolution of the Weyl points.

## III. RESULTS AND DISCUSSIONS

The crystal structure and Brillouin zone (BZ) of  $\text{Cu}_2\text{SnS}_3$  and  $\text{Cu}_2\text{SnSe}_3$  are shown in Fig. 1(a) and (b). They belong to the same space group *Imm2* (No. 44), which includes two mirror reflection symmetries  $M_x$  and  $M_y$  perpendicular to  $x$  and  $y$  axis, respectively, one twofold rotation symmetry  $C_{2z}$  along  $z$ -axis. It has time reversal symmetry (TRS)  $T$  but no inversion symmetry, which means the minimum number of Weyl nodes is four with two pairs in opposite chirality.

### A. $\text{Cu}_2\text{SnS}_3$

The band structure of  $\text{Cu}_2\text{SnS}_3$  calculated without SOC is shown in Fig. 1(c). The two mirror reflection symmetries  $M_x$  and  $M_y$  are represented by the colored planes in Fig. 1(b). We can find clearly that the band-crossing between the highest valence band and the lowest conduction band along the  $\Gamma$ -S and X- $\Gamma$  directions. According to the representation analysis of the symmetric operations, the conduction band and valence band forming the crossing node on path  $\Gamma$ -S have opposite eigenvalues of  $M_x$  and  $C_{2z}$  operators but the same eigenvalues of  $M_y$  operator. This means that the band-crossing is protected by the  $M_x$  and  $C_{2z}$  symmetries. The crossing point on the path X- $\Gamma$  is also protected by the  $M_x$  symmetry. By searching the entire BZ, we find that these band-crossing points form a closed nodal-ring around  $\Gamma$  on the  $M_x$  plane as shown in Fig. 1(e). Therefore, without SOC  $\text{Cu}_2\text{SnS}_3$  is the simplest TNLS with only one nodal ring.

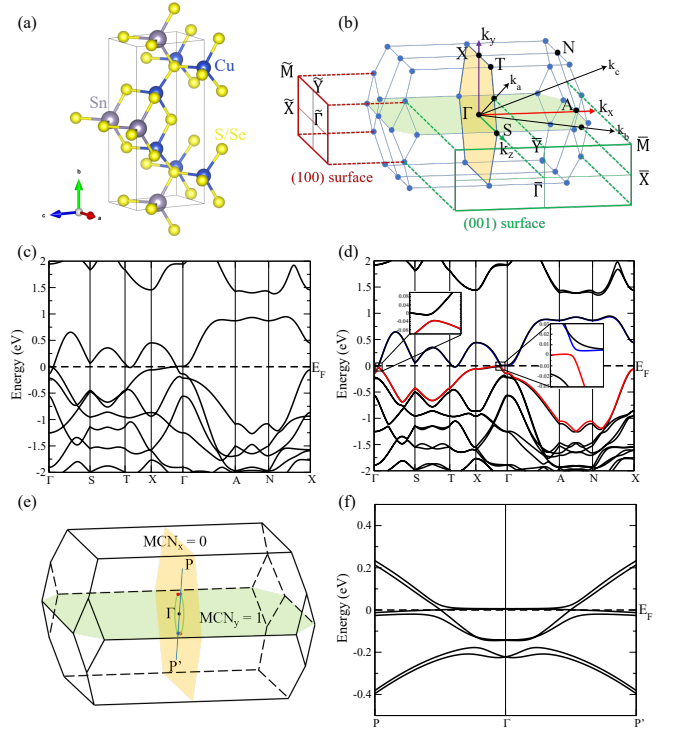


Figure 1. (a) The crystal structure of  $\text{Cu}_2\text{SnS}_3(\text{Se}_3)$ . The blue, grey and yellow balls represent Cu, Sn and S (Se) atoms, respectively. (b) The bulk BZ and the projected surface BZ for (001) and (100) surfaces. The light yellow and light green planes represent  $M_x$  and  $M_y$  planes, respectively. (c) and (d) The band structures of  $\text{Cu}_2\text{SnS}_3$  without and with SOC, respectively. (e) 3D schematic diagram of the nodal-ring (in the absence of SOC) and Weyl points (with SOC) in the BZ. The green line represents the nodal-ring. The blue and red dots denote the Weyl points with opposite chirality. (f) The band along the path passing through two Weyl points with the same chirality related with time-reversal symmetry. The path P to P' is shown in (e).

When SOC is taken into account, the crossing points on the above mentioned nodal ring are fully gapped. The band structure near the Fermi level is plotted in Fig. 1(d). However, there are two pairs of Weyl points created at the generic momenta on the  $k_z = 0$  plane. They are symmetric about the  $M_x$  and  $M_y$  planes. They also respect the  $C_{2z}$  rotation symmetry and TRS  $T$ . It is noted that  $k_z = 0$  plane is invariant under the joint operation  $C_{2z} * T$ , which results in 0 or  $\pi$  Berry phase for any loop in this plane.<sup>7,31</sup> The positions and chiralities of Weyl nodes are shown in Fig. 1(e). The bands along the  $k$  path which connects a pair of Weyl points with the same chirality to  $\Gamma$  point have been plotted in Fig. 1(f). The energy of Weyl points is very close to Fermi level, being about 1.4 meV above it.

It is noted that there is no topological indicator<sup>2,32,33</sup> that can be used to determine the topological classification in space group No. 44. Furthermore, spatial inversion symmetry is also absent so that Fu-Kane parity formula<sup>41-43</sup> is not applicable. To determine its topological phase, we take the Wilson loop method to calculate the  $Z_2$  invariant protected by

TRS  $T$  and the MCNs of mirror planes.<sup>17,34</sup> The MCN calculations for the two mirror planes are plotted in Fig. 2(a) and (b). They clearly show that MCN = 0 for  $M_x$  plane while MCN = 1 for  $M_y$  plane. To verify the results, we further calculate the flow of Wannier centers of all occupied states along half of the reciprocal lattice vector in the  $M_x$  and  $M_y$  planes, which can give out  $Z_2$  invariant protected by TRS. As shown in Fig. 2(c) and (d),  $Z_2$  is 0 for  $k_x = 0$  plane while 1 for  $k_y = 0$  plane, which is consistent with the MCN results. That the existence of Weyl node between two non-parallel mirror planes with different MCNs has been firstly pointed out and demonstrated in TaAs<sup>17</sup> and their influence on the pattern of Fermi arcs has also been discussed and studied experimentally in TaAs.<sup>44</sup> Therefore, the net topological charge of the Weyl nodes in one of the four blocks divided by these two mirror planes should be an odd number. In addition,  $k_z = 0$  plane is invariant under the joint operation of  $C_2 * T$ . Thus, there must be Weyl nodes in this plane, which is essentially the same as the constraint of in-plane Weyl nodes in inversion-symmetric magnetic space group with odd  $Z_4$  invariant and joint  $C_2 * T$  symmetry.<sup>7,31</sup>

The surface states and Fermi arcs of  $\text{Cu}_2\text{SnS}_3$  on (100) and (001) projected surfaces are plotted in Fig. 2(e)-(h). On the (001) surface, four Weyl points are all projected onto the surface separately. There are two Fermi arcs connecting the two pairs of Weyl points, respectively, which is clearly observed in the enlarged illustration of Fig. 2(f).  $\bar{\Gamma} - \bar{Y}$  and  $\bar{\Gamma} - \bar{X}$  line are the projection of  $M_x$  and  $M_y$  plane, respectively. Along the  $\bar{\Gamma} - \bar{X}$  line we can find a cross where the Fermi arc runs through it, which comes from MCN = 1 for the  $M_y$  plane. There is no Fermi arc crossing the  $\bar{\Gamma} - \bar{Y}$  line since MCN = 0 for the  $M_x$  plane. It is noted that if the Weyl nodes are off the  $k_z = 0$  plane, the number of Weyl nodes will be doubled and two Weyl nodes of the same chirality will be superposed on each other when projected onto (001) surface. The number of Fermi arcs connecting each projection should be two. The different MCNs for  $M_x$  and  $M_y$  planes limit that there must have odd number of Fermi arcs crossing  $\bar{\Gamma} - \bar{X}$  and even number of Fermi arcs crossing  $\bar{\Gamma} - \bar{Y}$ . Therefore, there is no way to satisfy all these constraints if assuming the Weyl nodes were off the  $k_z = 0$  plane.

On (100) surface, two opposite chiral Weyl nodes are projected to the same point on the  $\bar{\Gamma} - \bar{Y}$  line as shown in Fig. 2(h). Therefore, each projective point should be connected by two or zero Fermi arcs. Here,  $\bar{\Gamma} - \bar{X}$  line is the projection of  $M_y$  plane. We can still find that one Fermi arc sticking close to the bulk state crosses this line, which is consistent with MCN = 1 for  $M_y$  plane. In Fig. 2(g), the projected bulk Weyl points form solid Dirac cones with continuous eigen energies along  $\bar{\Gamma} - \bar{Y}$ . The surface states form an empty Dirac cone and have its Dirac node at  $\bar{\Gamma}$ . Along  $\bar{\Gamma} - \bar{Y}$ , both of its two branches merge into the solid Dirac cone where the bulk Weyl nodes are projected. Along  $\bar{\Gamma} - \bar{X}$ , there is only one branch connecting the bulk conduction bands and the other one merges into the valence states, which is consistent with MCN = 1 for  $M_y$ .

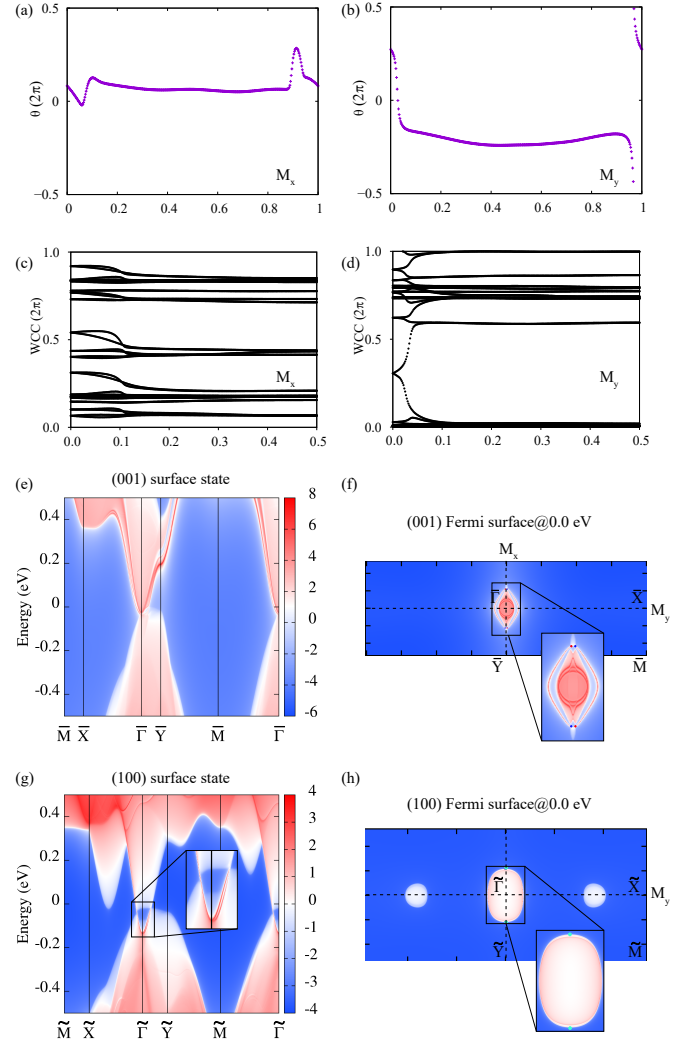


Figure 2. The calculated topological properties of  $\text{Cu}_2\text{SnS}_3$ . (a) and (b) The flow chart of the average position of the Wannier centers for occupied bands with mirror eigenvalue  $+i$  in the  $M_x$  (a) and  $M_y$  (b) planes. (c) and (d) The flow chart of the Wannier centers for all occupied bands in the  $M_x$  (c) and  $M_y$  (d) planes across half of the reciprocal lattice vector. (e) The surface states of (001) surface and (f) the corresponding Fermi surface; (g) The surface states of (100) surface and (h) the corresponding Fermi surface. The red and blue dots are the projections of opposite chiral Weyl points, respectively. The cyan dots are the superposition of two projected Weyl points with opposite chirality.

## B. $\text{Cu}_2\text{SnS}_3$

The band structures of  $\text{Cu}_2\text{SnS}_3$  without and with SOC are shown in Fig. 3(c) and (d), respectively. In the absence of SOC,  $\text{Cu}_2\text{SnS}_3$  is also a nodal-line semimetal with only one nodal ring centering at  $\bar{\Gamma}$  in the  $M_x$  plane. However, when SOC is taken into account, the band structure of  $\text{Cu}_2\text{SnS}_3$  is fully gapped at each  $k$  point along the nodal line. It can be looked as an insulator although there is no global gap in

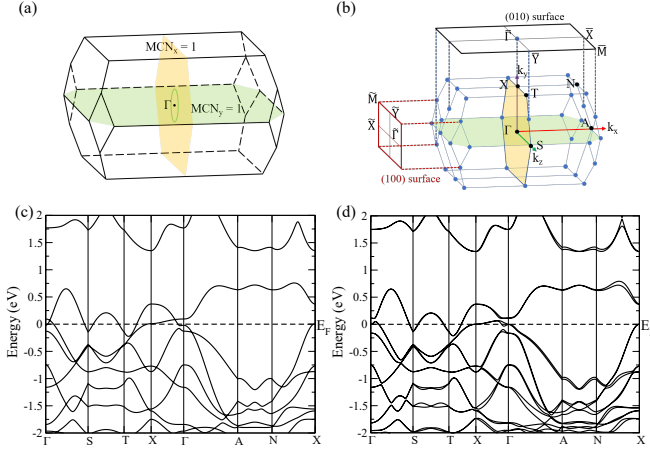


Figure 3. (a) 3D schematic diagram of the nodal-ring for  $\text{Cu}_2\text{SnSe}_3$  in the absence of SOC. (b) The bulk BZ and the projected surface BZ for (010) and (100) surfaces. (c) and (d) The band structures of  $\text{Cu}_2\text{SnSe}_3$  without and with SOC, respectively.

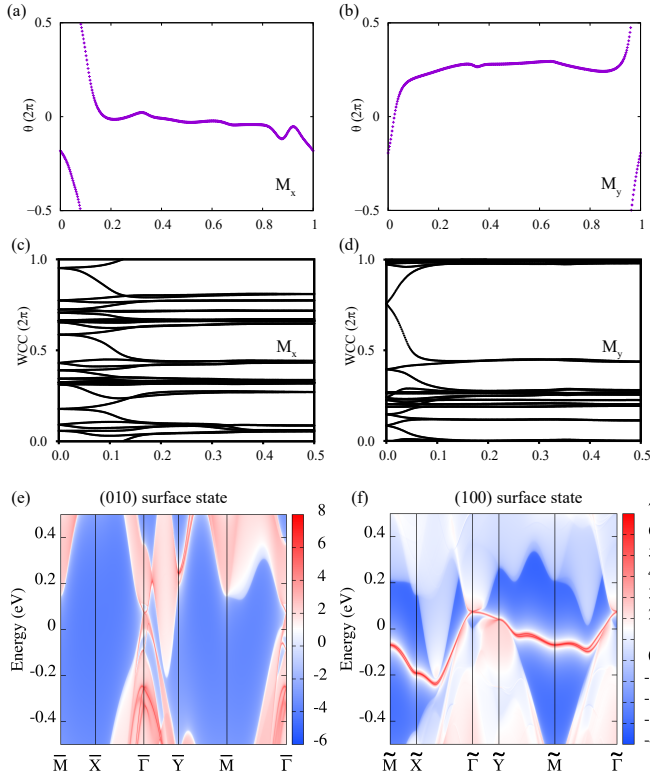


Figure 4. The calculation results of the topological properties of  $\text{Cu}_2\text{SnSe}_3$ . (a) and (b) The flow chart of the average position of the Wannier centers obtained by Wilson-loop calculation for bands with mirror eigenvalue  $i$  in the  $M_x$  (a) and  $M_y$  (b) planes. (c) and (d) The flow chart of the Wannier centers of all occupied states in the  $M_x$  (c) and  $M_y$  (d) planes along half of the reciprocal lattice vector. (e) and (f) The surface states of (010) projected surface and (100) projected surface, respectively.

the whole BZ. In order to determine whether it is a topologically nontrivial insulator, we further obtain the MCNs for  $M_x$  and  $M_y$  planes as shown in Fig. 4(a) and (b). It is obvious that  $\text{MCN} = 1$  for both of  $M_x$  and  $M_y$  planes, consistent with the  $Z_2$  invariant calculation shown in Fig. 4(c) and (d). Thus,  $\text{Cu}_2\text{SnSe}_3$  might be a WSM with even number of Weyl nodes in one quarter of the BZ divided by the  $M_x$  and  $M_y$  planes, or a strong TI with  $Z_2$  indices (1;000). We have found that the former situation is possible in another family member compound  $\text{Cu}_2\text{GeSe}_3$  as shown in the Appendix. The present compound  $\text{Cu}_2\text{SnSe}_3$  is the later case. The most typical feature of a TI is the appearance of odd number of Dirac cones on their surfaces. We further calculate the (010) and (100) surface states of  $\text{Cu}_2\text{SnSe}_3$  as shown in Fig. 4(e) and (f). There is one Dirac cone at  $\tilde{\Gamma}$  point on either (010) or (100) surface and the two branches of the Dirac cone connecting the valence and conduction bands, respectively.

#### IV. TOPOLOGICAL PHASE TRANSITION

As the materials of a family with the same space group,  $\text{Cu}_2\text{SnS}_3$  and  $\text{Cu}_2\text{SnSe}_3$  are both topological nodal ring semimetals when SOC is not taken into account, but they are obviously different in band topology when SOC is considered. It is intriguing to know about the mechanism underlying this difference. Therefore, we're going to explore the process of TPT between them continuously from a WSM to a TI by doping Se into  $\text{Cu}_2\text{SnS}_3$ , through which the strength of SOC can be tuned.

We use the virtual crystal approximation (VCA) method to calculate the bands of  $\text{Cu}_2\text{SnS}_{3-x}\text{Se}_x$  to simulate Se doping effect as shown in Fig. 5(a)-(d). The change in lattice constants is linearly scaled between  $\text{Cu}_2\text{SnS}_3$  and  $\text{Cu}_2\text{SnSe}_3$  with the doping concentration. It can be seen that the band inversion between the valence band and conduction band around  $\Gamma$  keeps existing as Se doping ratio increases, and the spin splitting in these bands also increases due to enhanced SOC. This indicates the SOC is tunable. In order to accurately determine where the phase transition has occurred, we calculated the MCN and  $Z_2$  for  $M_x$  plane in different doping cases. We find that when S:Se = 0.9:0.1, MCN and  $Z_2$  on  $M_x$  plane are both zero. When S:Se = 0.6:0.4, both of MCN and  $Z_2$  on  $M_x$  plane become one, as shown in Fig. 5(e)-(f), indicating that TPT has occurred around this point.

This work presents a simple and ideal model material system for realizing the TPT proposed by S. Murakami<sup>28</sup>. The process of Weyl nodes annihilation in pair and the TPT from a WSM to a TI are shown in Fig. 6(a). This is further simulated by using the linear mixing of the tight-binding Hamiltonians of  $\text{Cu}_2\text{SnS}_3$  and  $\text{Cu}_2\text{SnSe}_3$  constructed from the generated Wannier functions. We find that the Weyl points gradually approach the  $k_x = 0$  plane along the trajectory when the Se doping ratio increases as shown in Fig. 6(b). According to the calculation results, we find that at about S:Se = 0.63:0.37 the Weyl points finally annihilate on the  $k_x = 0$  plane and TPT from a WSM to a TI is realized with the  $\text{MCN} = 0$  for  $M_x$ . The critical value of S:Se determined from linear mixing of tight-



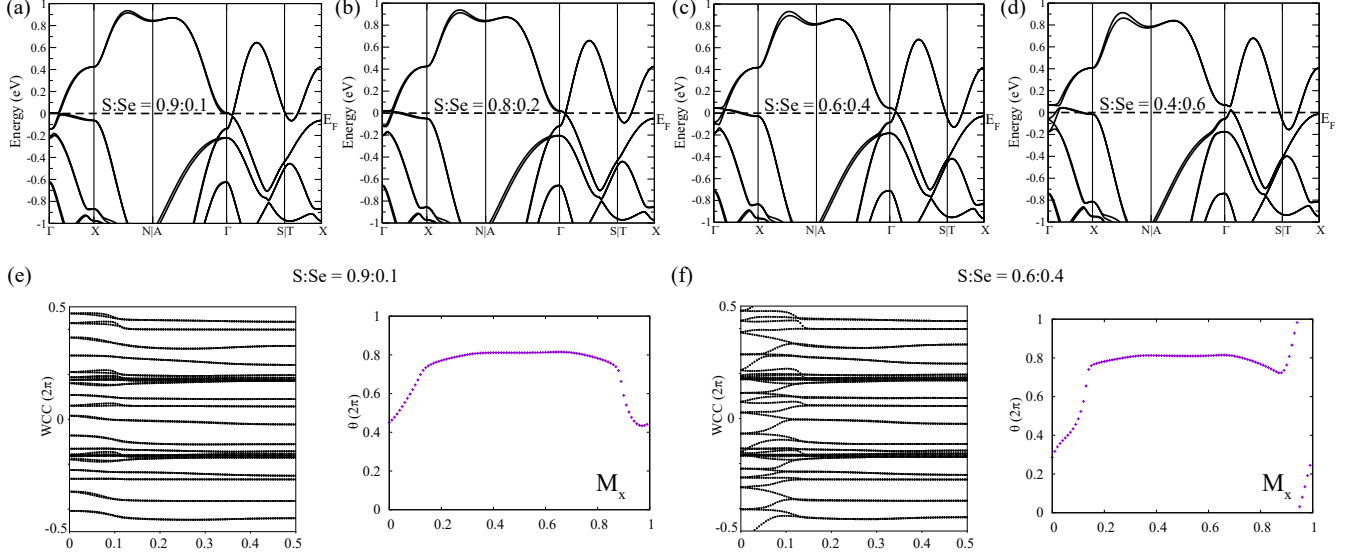


Figure 5. (a)-(d) Band structures calculated by VCA method with different value of S:Se ratio. (e)-(f) The flow of Wannier centers and mirror Chern numbers of  $M_x$  plane with different S:Se ratio values.

binding Hamiltonian is nearly the same as the first-principles calculation from VCA.

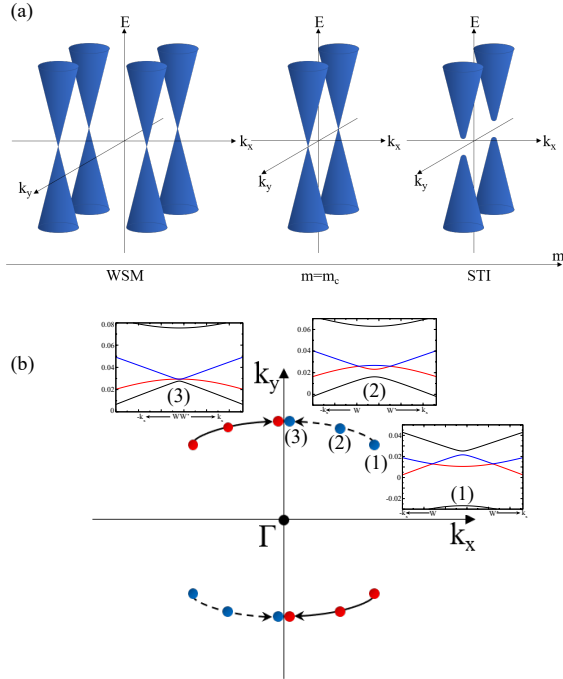


Figure 6. (a) Schematic evolution of the topological phase transition from Cu<sub>2</sub>SnS<sub>3</sub> (WSM) to Cu<sub>2</sub>SnSe<sub>3</sub> (STI). (b) Band structures of Cu<sub>2</sub>SnS<sub>3-x</sub>Se<sub>x</sub> calculated by linear mixing of Wannier Hamiltonians with Se doping of 0.0 (1), 0.3 (2), and 0.365 (3). The  $k$ -path passes through the two Weyl points with opposite chirality along the  $k_x$ -axis.

In order to further understand the TPT, we construct a two-band  $k \cdot p$  model, which describes the bands around the crossing point between nodal-ring and  $k_z$  axis in case without SOC. According to the band representations at this crossing point, the Hamiltonian expanded around it with momentum  $q(q_x, q_y, q_z)$  can be simply written as:

$$H_0(q) = q_x \tau_x + q_y^2 \tau_z + q_z \tau_z$$

, where  $q_x$ ,  $q_y$  and  $q_z$  are along  $k_x$ ,  $k_y$  and  $k_z$  axis, respectively. In the absence of SOC, the Hamiltonian has linear dispersion along the  $q_x$  and  $q_z$ -axis, but quadratic one along the  $q_y$ -axis.

When SOC is further included, the two-band  $k \cdot p$  model should become a four-band model because of the spin degree of freedom. At the zero point of  $q$ , the generators of the little group have  $C_{2z}$ ,  $M_x$  and  $M_y$  symmetries. Their matrix representations can be obtained from the results of first-principles calculations:

$$M_x = i\tau_z \otimes s_x,$$

$$M_y = i\tau_0 \otimes s_y,$$

$$C_{2z} = i\tau_z \otimes s_z.$$

When SOC is considered, the spin components should be added to the previous model, which is equivalent to adding new mass terms to the original Hamiltonian. The mass term must commute with  $C_{2z}$ ,  $M_x$  and  $M_y$ . So the new Hamiltonian is given by:

$$H(q) = q_x \tau_x + q_y^2 \tau_z + q_z \tau_z + m \tau_y s_y$$

For states in the  $M_x$  plane, applying operation  $M_x$  to  $H(q_x = 0)$ , we can get the block diagonal matrix of  $H(q_y, q_z)$  in the  $i$  or  $-i$  eigenvalue subspaces of  $M_x$ <sup>45,46</sup>:

$$UM_xU^{-1} = \begin{pmatrix} i & 0 & 0 & 0 \\ 0 & i & 0 & 0 \\ 0 & 0 & -i & 0 \\ 0 & 0 & 0 & -i \end{pmatrix} \quad (1)$$

$$UH(q_y, q_z)U^{-1} = \begin{pmatrix} -q_y^2 - q_z & -m & 0 & 0 \\ -m & q_y^2 + q_z & 0 & 0 \\ 0 & 0 & -q_y^2 - q_z & m \\ 0 & 0 & m & q_y^2 + q_z \end{pmatrix} \quad (2)$$

The subspace Hamiltonian of  $\pm i$  eigenvalue is

$$H_{yz}^{\pm i}(q) = \mathbf{d} \cdot \sigma = \mp m\sigma_x - (q_y^2 + q_z)\sigma_z,$$

and the MCN for  $M_x$  plane is

$$C_{M_x}^{\pm i} = \frac{1}{4\pi} \int dq_y dq_z \hat{\mathbf{d}} \cdot (\partial_{q_y} \hat{\mathbf{d}} \times \partial_{q_z} \hat{\mathbf{d}}) = 0.$$

Obviously, in  $i$  or  $-i$  subspace, MCN = 0 on  $M_x$  plane, which means that the  $H_{yz}(q)$  is trivial.

However, for  $M_y$  plane, we can obtain the nontrivial matrix of  $H(q_x, q_z)$  by applying  $M_y$  to  $H(q_y = 0)$ .

$$U'H(q_x, q_z)U'^{-1} = \begin{pmatrix} -q_z & q_x + im & 0 & 0 \\ q_x - im & q_z & 0 & 0 \\ 0 & 0 & -q_z & q_x - im \\ 0 & 0 & q_x + im & q_z \end{pmatrix} \quad (3)$$

The subspace Hamiltonian of  $\pm i$  eigenvalue is

$$H_{xz}^{\pm i}(q) = \mathbf{d} \cdot \sigma = q_x\sigma_x \mp m\sigma_y - q_z\sigma_z,$$

and the MCN for  $M_y$  is

$$C_{M_y}^{\pm i} = \frac{1}{4\pi} \int dq_x dq_z \hat{\mathbf{d}} \cdot (\partial_{q_x} \hat{\mathbf{d}} \times \partial_{q_z} \hat{\mathbf{d}}) = \mp \frac{1}{2} \text{sgn}(m).$$

Since there are two crossing points on the  $M_y$  plane because of the TRS without SOC, the mirror Chern number is

$$C_{M_y} = |C_{M_y}^{\pm i}| \times 2 = 1.$$

These results are consistent with those of  $\text{Cu}_2\text{SnS}_3$  from first-principles calculations.

## V. SUMMARY

Through first-principles calculations, we have proposed that  $\text{Cu}_2\text{SnS}_3$  and  $\text{Cu}_2\text{SnSe}_3$  can be used to model the topological phase transition from a WSM to a TI. In the absence of SOC, both of them are the simplest nodal line semimetal with only a single nodal ring centering at  $\Gamma$ , which is protected by  $M_x$  symmetry and lies in the mirror plane. When SOC is

taken into account, they are quite different. For  $\text{Cu}_2\text{SnS}_3$ , the nodal-ring evolves into two pairs of Weyl points in the  $k_z = 0$  plane, as indicated by the different MCN for  $M_x$  and  $M_y$  planes, namely MCN = 0 for  $M_x$  and MCN = 1 for  $M_y$  plane. For  $\text{Cu}_2\text{SnSe}_3$ , the nodal-ring is fully gapped and the system becomes a strong TI, as indicated by the same MCN = 1 for both  $M_x$  and  $M_y$  planes. The difference in them comes from the different strength of effective SOC which can be systematically tuned by doping Se into  $\text{Cu}_2\text{SnS}_3$ . Employing VCA, we have simulated the doping concentration continuously to show the movement of Weyl points and their annihilation in the  $M_x$  plane during the TPT. The critical doping level is S:Se = 0.63:0.37. We have also constructed a  $k \cdot p$  model to explain these results. Here, it must be noted that all the above results on specific materials are based on the GGA calculations, which usually overestimates the band inversion. The previous work<sup>47-49</sup> mentioned that  $\text{Cu}_2\text{SnS}_3$  and  $\text{Cu}_2\text{SnSe}_3$  are gapped insulators in reality and our improved hybrid functional (HSE06) calculations shown in Appendix are consistent with them. There are still some family compounds, like  $\text{Cu}_2\text{SiTe}_3$ ,  $\text{Cu}_2\text{GeSe}_3$ ,  $\text{Cu}_2\text{GeTe}_3$ , and  $\text{Cu}_2\text{SnTe}_3$ , keeping the band inversion and their band topology can be analyzed similarly. Nevertheless, our work is of importance and usefulness for theoretically studying the topological states and phase transitions among them.

## VI. ACKNOWLEDGEMENT

We acknowledge the supports from the National Natural Science Foundation (Grant No. 11925408, 11974076, 11921004 and 12188101), the Ministry of Science and Technology of China (Grant No. 2018YFA0305700), the Chinese Academy of Sciences (Grant No. XDB33000000), the K. C. Wong Education Foundation (GJTD-2018-01), the Beijing Natural Science Foundation (Z180008), and the Beijing Municipal Science and Technology Commission (Z191100007219013). CY is supported by the Swiss National Science Foundation (200021-196966). WZ is supported by the Key Project of Natural Science Foundation of Fujian Province (2021J02012).

### Appendix A: Band structures of the other members in $\text{Cu}_2\text{SnS}_3$ family

In this section, we present the bulk band structures of the other members in  $\text{Cu}_2\text{SnS}_3$  family without and with spin-orbit coupling (SOC), which are all calculated by GGA.

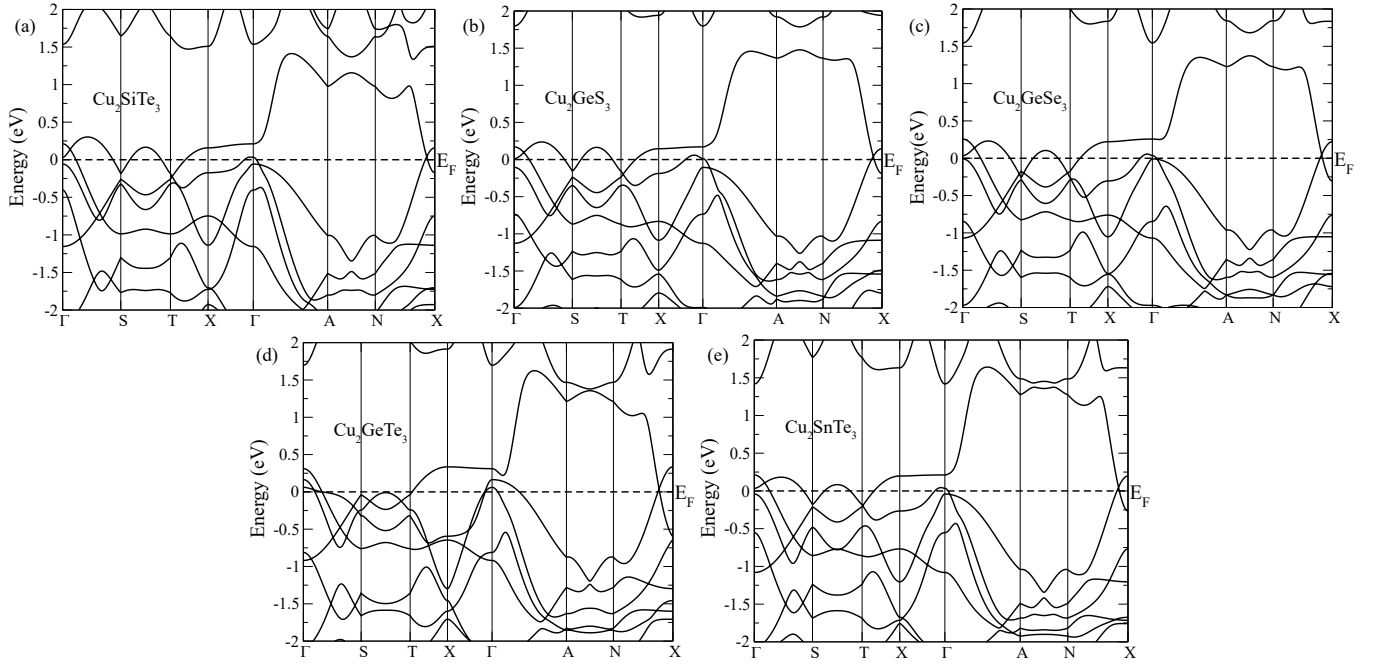


Figure 7. Band structures of  $\text{Cu}_2\text{SiTe}_3$ ,  $\text{Cu}_2\text{GeS}_3$ ,  $\text{Cu}_2\text{GeSe}_3$ ,  $\text{Cu}_2\text{GeTe}_3$  and  $\text{Cu}_2\text{SnTe}_3$  along high symmetry points without the spin-orbit coupling.

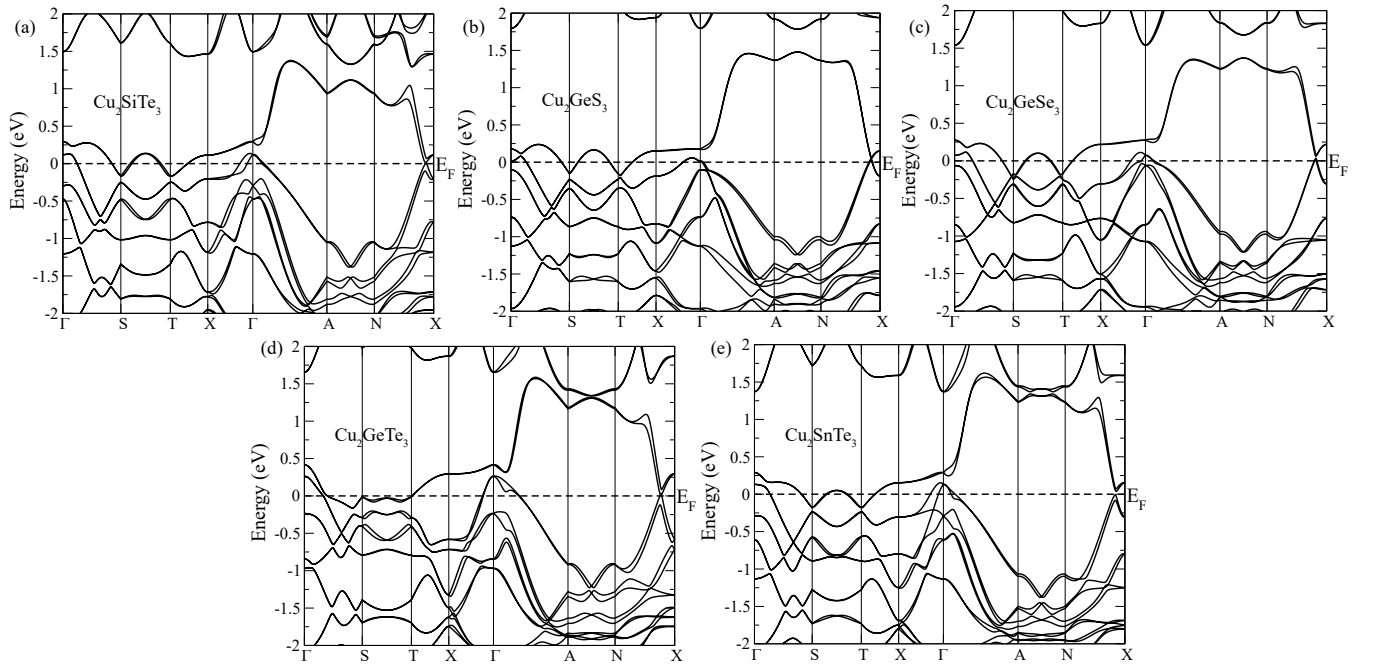


Figure 8. Band structures of  $\text{Cu}_2\text{SiTe}_3$ ,  $\text{Cu}_2\text{GeS}_3$ ,  $\text{Cu}_2\text{GeSe}_3$ ,  $\text{Cu}_2\text{GeTe}_3$  and  $\text{Cu}_2\text{SnTe}_3$  along high symmetry points with the spin-orbit coupling.

### Appendix B: MCNs of $M_x$ and $M_y$ planes for other materials of $\text{Cu}_2\text{SnS}_3$ family

In this section, we give the MCNs of  $M_x$  and  $M_y$  planes for other materials of  $\text{Cu}_2\text{SnS}_3$  family. It's obvious to see that all the members have  $\text{MCN} = 1$  for  $M_y$  plane, but for  $M_x$  plane, except for  $\text{Cu}_2\text{SnS}_3$ , all the other members have  $\text{MCN} = 1$ . This is a very novel phenomenon.

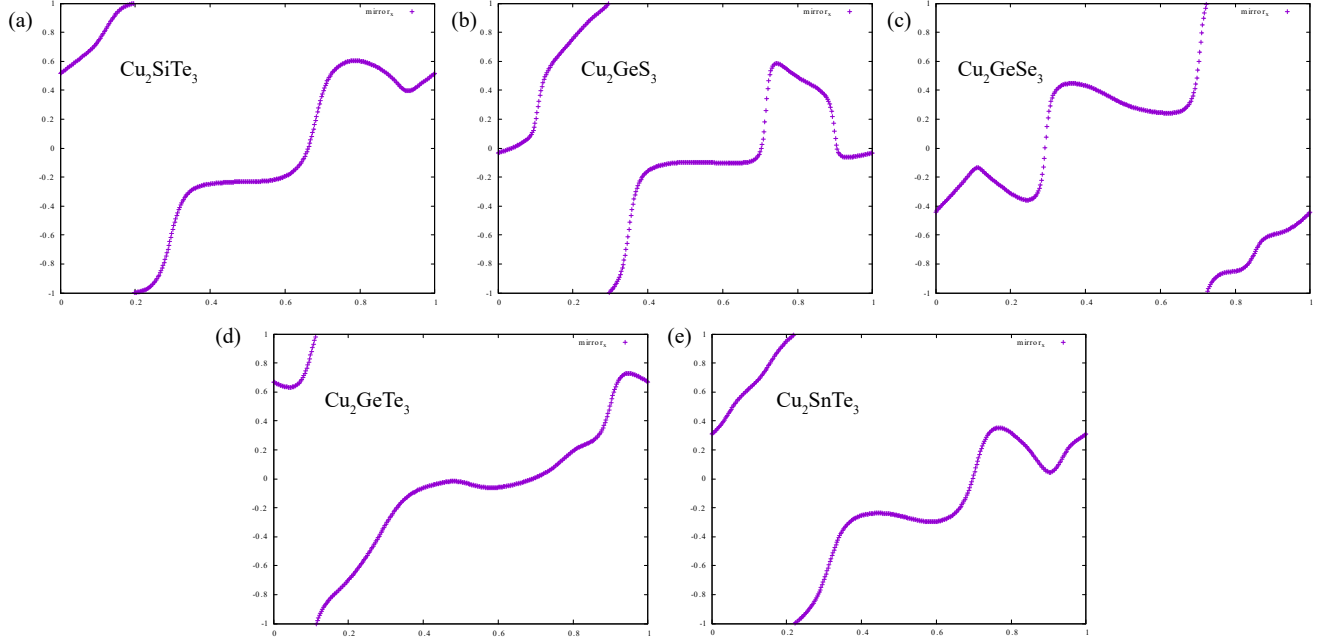


Figure 9. Mirror Chern numbers (MCN) of  $\text{Cu}_2\text{SiTe}_3$ ,  $\text{Cu}_2\text{GeS}_3$ ,  $\text{Cu}_2\text{GeSe}_3$ ,  $\text{Cu}_2\text{GeTe}_3$  and  $\text{Cu}_2\text{SnTe}_3$  for  $M_x$  plane.

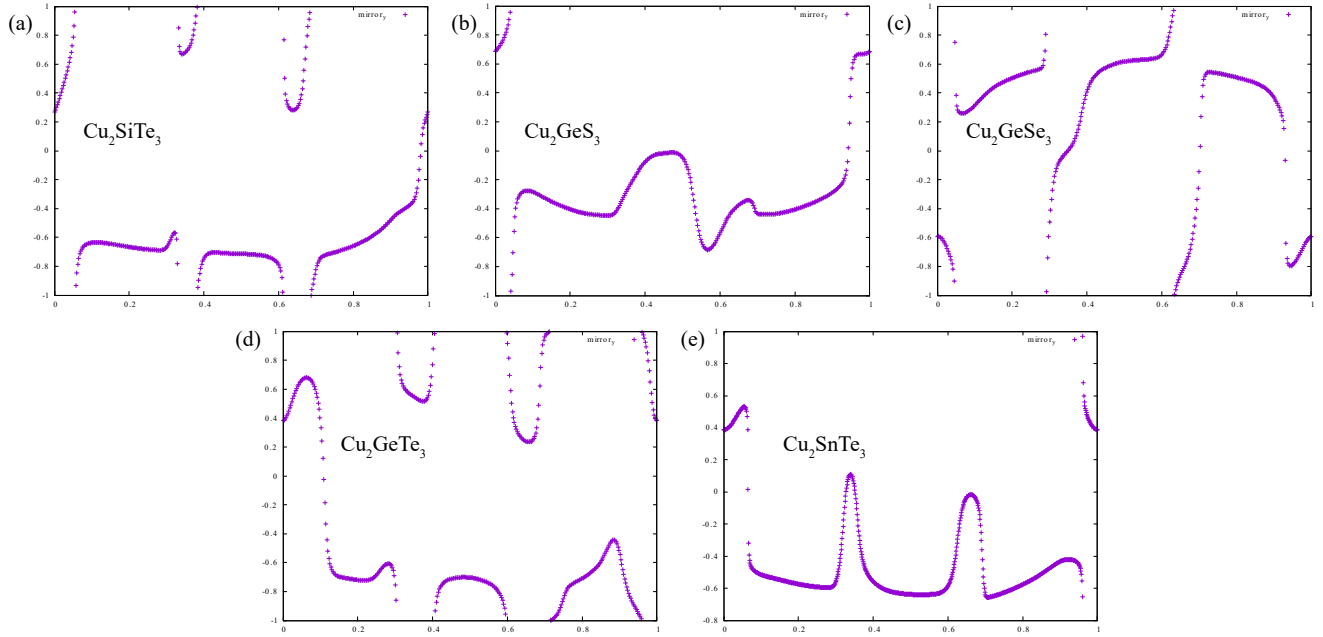


Figure 10. Mirror Chern numbers (MCN) of  $\text{Cu}_2\text{SiTe}_3$ ,  $\text{Cu}_2\text{GeS}_3$ ,  $\text{Cu}_2\text{GeSe}_3$ ,  $\text{Cu}_2\text{GeTe}_3$  and  $\text{Cu}_2\text{SnTe}_3$  for  $M_y$  plane.



### Appendix C: The distribution of Weyl points in $\text{Cu}_2\text{SnS}_3$ family

In this section, we give the position of Weyl points for these materials of  $\text{Cu}_2\text{SnS}_3$  family.

Table I. The distribution of Weyl points in  $\text{Cu}_2\text{SnS}_3$  family.

material	a (Å)	b (Å)	c (Å)	Weyl points ( $k_x, k_y, k_z$ ) ( $2\pi/a$ )	energy (eV)	number
$\text{Cu}_2\text{SiTe}_3$	4.2527	12.5882	5.9446	upper and lower surfaces of BZ		8 small nodal-rings
$\text{Cu}_2\text{GeS}_3$	3.7660	11.3210	5.2100	(0.0510, 0.4044, 0.3047)	-0.0749	8
				(0.0287, 0.2935, 0.2154)	0.0062	8
$\text{Cu}_2\text{GeSe}_3$	3.9600	11.8600	5.4850	(0.0617, 0.3173, 0.2536)	-0.0111	8
$\text{Cu}_2\text{GeTe}_3$	4.2115	12.6410	5.9261	(0.1313, 0.0775, 0.1327)	0.1290	8
				upper and lower surfaces of BZ		4 large nodal-rings
$\text{Cu}_2\text{SnS}_3$	3.8937	11.5720	5.4436	(0.0061, 0.1120, 0.0000)	0.0014	4
$\text{Cu}_2\text{SnSe}_3$	4.1158	12.2715	5.7528	Topological insulator (TI)		0
$\text{Cu}_2\text{SnTe}_3$	4.2740	12.8330	6.0430	(0.0576, 0.1502, 0.1226)	0.0748	8
				(0.0782, 0.4763, 0.3110)	-0.1824	8

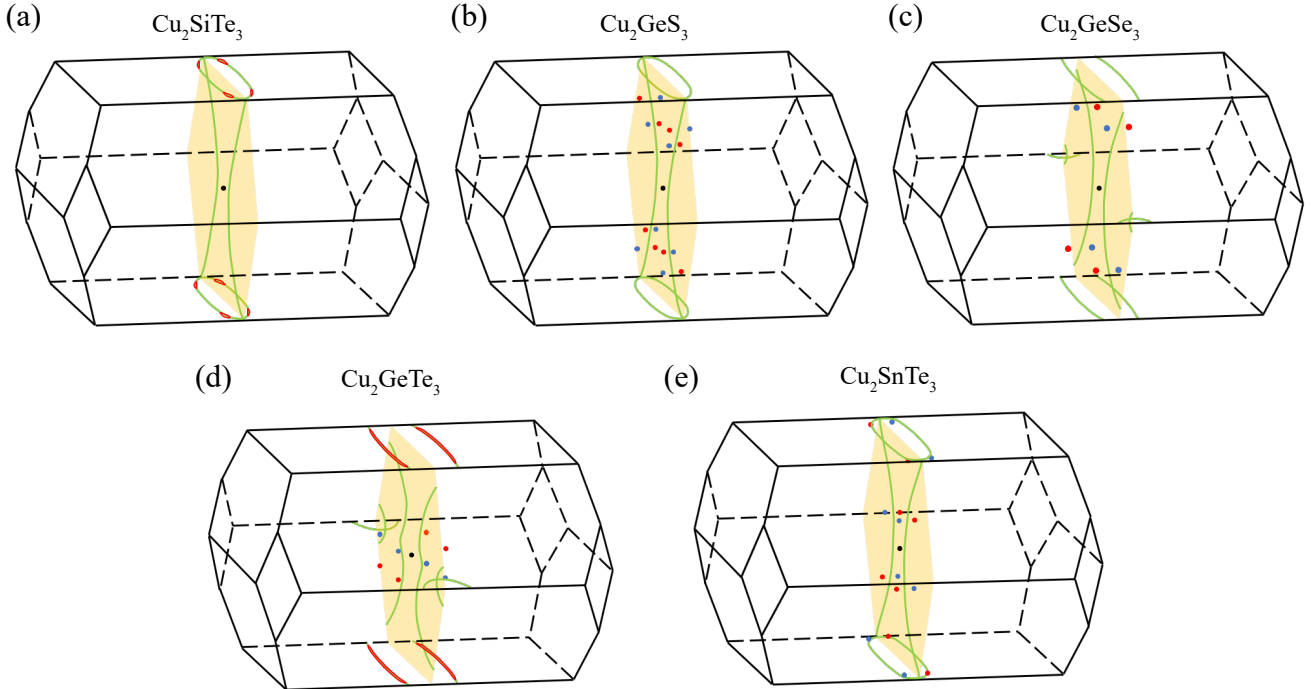


Figure 11. The schematic diagrams of Weyl points distribution of  $\text{Cu}_2\text{SiTe}_3$ ,  $\text{Cu}_2\text{GeS}_3$ ,  $\text{Cu}_2\text{GeSe}_3$ ,  $\text{Cu}_2\text{GeTe}_3$ , and  $\text{Cu}_2\text{SnTe}_3$  (The green line represents the nodal-chain and nodal-ring. The blue dots denote the Weyl points with negative chirality and the red dots denote the Weyl points with positive chirality).

### Appendix D: Band structures of $\text{Cu}_2\text{SnS}_3$ family with HSE06

In this section, we show the bands calculation results with HSE06 for all materials without SOC and partial materials with SOC.

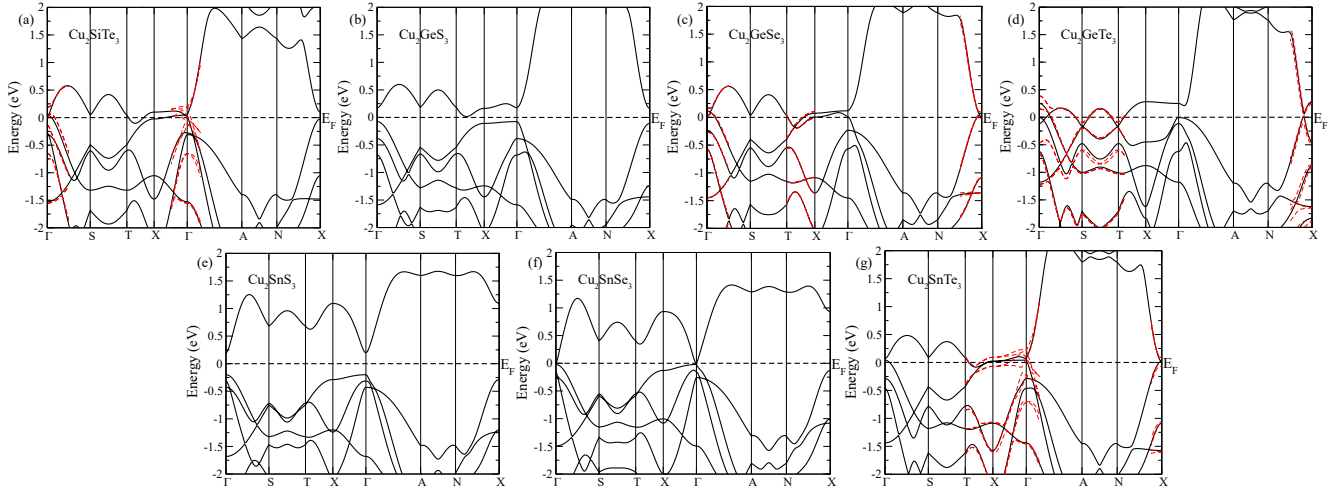


Figure 12. The band structures of  $\text{Cu}_2\text{SiTe}_3$ ,  $\text{Cu}_2\text{GeS}_3$ ,  $\text{Cu}_2\text{GeSe}_3$ ,  $\text{Cu}_2\text{GeTe}_3$ ,  $\text{Cu}_2\text{SnS}_3$ ,  $\text{Cu}_2\text{SnSe}_3$  and  $\text{Cu}_2\text{SnTe}_3$  with HSE06 along high symmetry points without the spin-orbit coupling (The red dotted lines in part of the figures are the bands with SOC for comparison).

- \* zhangw721@163.com  
† cfang@iphy.ac.cn  
‡ hmweng@iphy.ac.cn
- <sup>1</sup> A. P. Schnyder, S. Ryu, A. Furusaki, and A. W. W. Ludwig, *Phys. Rev. B* **78**, 195125 (2008).
  - <sup>2</sup> Z. Song, T. Zhang, Z. Fang, and C. Fang, *Nature communications* **9**, 1 (2018).
  - <sup>3</sup> T. Zhang, Y. Jiang, Z. Song, H. Huang, Y. He, Z. Fang, H. Weng, and C. Fang, *Nature* **566**, 475 (2019).
  - <sup>4</sup> M. Vergniory, L. Elcoro, C. Felser, N. Regnault, B. A. Bernevig, and Z. Wang, *Nature* **566**, 480 (2019).
  - <sup>5</sup> F. Tang, H. C. Po, A. Vishwanath, and X. Wan, *Nature* **566**, 486 (2019).
  - <sup>6</sup> Y. Xu, L. Elcoro, Z.-D. Song, B. J. Wieder, M. Vergniory, N. Regnault, Y. Chen, C. Felser, and B. A. Bernevig, *Nature* **586**, 702 (2020).
  - <sup>7</sup> B. Peng, Y. Jiang, Z. Fang, H. Weng, and C. Fang, (2021), [arXiv:2102.12645 \[cond-mat.mes-hall\]](https://arxiv.org/abs/2102.12645).
  - <sup>8</sup> J. Kruthoff, J. de Boer, J. van Wezel, C. L. Kane, and R.-J. Slager, *Phys. Rev. X* **7**, 041069 (2017).
  - <sup>9</sup> A. Bouhon, G. F. Lange, and R.-J. Slager, *Phys. Rev. B* **103**, 245127 (2021).
  - <sup>10</sup> M. Z. Hasan and C. L. Kane, *Rev. Mod. Phys.* **82**, 3045 (2010).
  - <sup>11</sup> X.-L. Qi and S.-C. Zhang, *Rev. Mod. Phys.* **83**, 1057 (2011).
  - <sup>12</sup> X. Wan, A. M. Turner, A. Vishwanath, and S. Y. Savrasov, *Phys. Rev. B* **83**, 205101 (2011).
  - <sup>13</sup> A. A. Burkov and L. Balents, *Phys. Rev. Lett.* **107**, 127205 (2011).
  - <sup>14</sup> S. M. Young, S. Zaheer, J. C. Y. Teo, C. L. Kane, E. J. Mele, and A. M. Rappe, *Phys. Rev. Lett.* **108**, 140405 (2012).
  - <sup>15</sup> J. L. Mañes, *Phys. Rev. B* **85**, 155118 (2012).
  - <sup>16</sup> B.-J. Yang and N. Nagaosa, *Nature communications* **5**, 1 (2014).
  - <sup>17</sup> H. Weng, C. Fang, Z. Fang, B. A. Bernevig, and X. Dai, *Phys. Rev. X* **5**, 011029 (2015).
  - <sup>18</sup> H. Weng, Y. Liang, Q. Xu, R. Yu, Z. Fang, X. Dai, and Y. Kawa-zoe, *Phys. Rev. B* **92**, 045108 (2015).
  - <sup>19</sup> N. P. Armitage, E. J. Mele, and A. Vishwanath, *Rev. Mod. Phys.* **90**, 015001 (2018).
  - <sup>20</sup> H. Weng, R. Yu, X. Hu, X. Dai, and Z. Fang, *Advances in Physics* **64**, 227 (2015).
  - <sup>21</sup> H. Weng, X. Dai, and Z. Fang, *Journal of Physics: Condensed Matter* **28**, 303001 (2016).
  - <sup>22</sup> H. Weng, C. Fang, Z. Fang, and X. Dai, *National Science Review* **4**, 798 (2017).
  - <sup>23</sup> A. Bernevig, H. Weng, Z. Fang, and X. Dai, *Journal of the Physical Society of Japan* **87**, 041001 (2018).
  - <sup>24</sup> C. Fang, H. Weng, X. Dai, and Z. Fang, *Chinese Physics B* **25**, 117106 (2016).
  - <sup>25</sup> S. Murakami, *New Journal of Physics* **9**, 356 (2007).
  - <sup>26</sup> S. Murakami, S. Iso, Y. Avishai, M. Onoda, and N. Nagaosa, *Phys. Rev. B* **76**, 205304 (2007).
  - <sup>27</sup> S. Murakami and S.-i. Kuga, *Phys. Rev. B* **78**, 165313 (2008).
  - <sup>28</sup> S. Murakami, *Physica E: Low-dimensional Systems and Nanostructures* **43**, 748 (2011).
  - <sup>29</sup> R. Okugawa and S. Murakami, *Phys. Rev. B* **89**, 235315 (2014).
  - <sup>30</sup> S. Murakami, M. Hirayama, R. Okugawa, and T. Miyake, *Science Advances* **3** (2017), 10.1126/sciadv.1602680.
  - <sup>31</sup> Y. Hu, C. Yue, D. Yuan, J. Gao, Z. Huang, Z. Fang, C. Fang, H. Weng, and W. Zhang, (2021), [arXiv:2112.04127 \[cond-mat.mtrl-sci\]](https://arxiv.org/abs/2112.04127).
  - <sup>32</sup> H. C. Po, A. Vishwanath, and H. Watanabe, *Nature communications* **8**, 1 (2017).
  - <sup>33</sup> Z. Song, T. Zhang, and C. Fang, *Phys. Rev. X* **8**, 031069 (2018).
  - <sup>34</sup> R. Yu, X. L. Qi, A. Bernevig, Z. Fang, and X. Dai, *Phys. Rev. B* **84**, 075119 (2011).
  - <sup>35</sup> D. Gresch, G. Autès, O. V. Yazyev, M. Troyer, D. Vanderbilt, B. A. Bernevig, and A. A. Soluyanov, *Phys. Rev. B* **95**, 075146 (2017).
  - <sup>36</sup> G. Kresse and J. Furthmüller, *Computational materials science* **6**, 15 (1996).
  - <sup>37</sup> P. E. Blöchl, *Phys. Rev. B* **50**, 17953 (1994).
  - <sup>38</sup> J. P. Perdew, K. Burke, and M. Ernzerhof, *Phys. Rev. Lett.* **77**, 3865 (1996).
  - <sup>39</sup> A. A. Mostofi, J. R. Yates, Y.-S. Lee, I. Souza, D. Vanderbilt, and N. Marzari, *Computer physics communications* **178**, 685 (2008).

- <sup>40</sup> Q. Wu, S. Zhang, H.-F. Song, M. Troyer, and A. A. Soluyanov, *Computer Physics Communications* **224**, 405 (2018).
- <sup>41</sup> C. L. Kane and E. J. Mele, *Phys. Rev. Lett.* **95**, 146802 (2005).
- <sup>42</sup> L. Fu, C. L. Kane, and E. J. Mele, *Phys. Rev. Lett.* **98**, 106803 (2007).
- <sup>43</sup> L. Fu and C. L. Kane, *Phys. Rev. B* **76**, 045302 (2007).
- <sup>44</sup> B. Q. Lv, H. M. Weng, B. B. Fu, X. P. Wang, H. Miao, J. Ma, P. Richard, X. C. Huang, L. X. Zhao, G. F. Chen, Z. Fang, X. Dai, T. Qian, and H. Ding, *Phys. Rev. X* **5**, 031013 (2015).
- <sup>45</sup> T. H. Hsieh, H. Lin, J. Liu, W. Duan, A. Bansil, and L. Fu, *Nature communications* **3**, 982 (2012).
- <sup>46</sup> T. H. Hsieh, J. Liu, and L. Fu, *Phys. Rev. B* **90**, 081112 (2014).
- <sup>47</sup> S. G. Choi, J. Kang, J. Li, H. Haneef, N. J. Podraza, C. Beall, S.-H. Wei, S. Christensen, and I. L. Repins, *Applied Physics Letters* **106**, 043902 (2015).
- <sup>48</sup> M. Mesbahi, M. L. Benkhedir, and I. Conversion, *UPB Sci. Bull., Series A* **79** (2017).
- <sup>49</sup> Y. Zhou, H. Wu, D. Wang, L. Fu, Y. Zhang, J. He, S. Pennycook, and L.-D. Zhao, *Materials Today Physics* **7**, 77 (2018).